RSC Advances

PAPER

View Article Online
View Journal | View Issue

Cite this: *RSC Adv.*, 2026, **16**, 15204

In situ synthesis of MXene@Iron oxide nanoparticle composites *via* pulsed laser ablation in liquid applied for electrochemical H_2O_2 reduction

Lenka Lorencová,[ab] Eva Noskovičová,[bc] Monika Jerigová,[bc] Monika Stupavská,[d] Ľubomír Orovčík,[e] Lucia Kopčanová,[e] Peter Kasák,[f] Andrej Vikartovský,[ag] Dušan Lorenc,[ch] Khaled A. Mahmoud[i] and Ján Tkáč *[a]

We propose to circumvent the lack of intrinsic magnetism in MXenes by *in situ* decorating the samples with magnetic nanoparticles during laser ablation in liquid by deposition of iron species on three types of MXenes (nanocomposites). The basic properties of such nanocomposites were characterized by a number of techniques including Scanning Electron Microscopy (SEM), Secondary Ion Mass Spectrometry (SIMS), X-ray Photoelectron Spectroscopy (XPS), electrochemical investigation and the optical Faraday effect. The results indicate significant differences in the content of Fe species deposited on MXenes ($Ti_3C_2T_x$; Nb_2CT_x and $Nb_4C_3T_x$) and the amount of Fe species deposited on MXenes is triggered by the density of plasmons present within MXenes. Moreover, we confimed a correlation between the capability of MXene-based Fe nanocomposites to electrochemically reduce hydrogen peroxide and electrochemical activity of Fe species present on MXenes. The highest electrochemical current density obtained for H_2O_2 reduction was obtained on the $Ti_3C_2T_x$ MXene-based Fe nanocomposite with the value of 4399 μA cm^{-2}. We further discuss how to improve the current density obtained for H_2O_2 reduction on the other MXene-based Fe nanocomposites (Nb_2CT_x and $Nb_4C_3T_x$) using alternative synthesis protocols.

Received 17th January 2026
Accepted 4th March 2026

DOI: 10.1039/d6ra00426a

rsc.li/rsc-advances

Introduction

Over the last decade, MXenes[1,2] have become prominent two-dimensional nanomaterials due to their advantageous physical and chemical properties. Their application scope[3–13] has expanded considerably, driven by ease of processing and compositional versatility that yield favorable electronic,[14,15] optical,[16,17] mechanical,[18,19] antimicrobial,[20,21] electrocatalytic,[22,23] thermal,[24,25] and magnetic properties.[26,27] Their attractiveness is further reinforced by inherent hydrophilicity, tunable surface chemistry, high flake availability, and favorable synthesis yields.[28] Recent advances have focused on patterning techniques to create functional MXene-based materials with enhanced performance.[29–31]

However, most MXenes lack spontaneous magnetism due to strong covalent M–X and M–T bonds,[26] as evidenced by the limited intrinsic magnetic response of Ti_3C_2 and Nb_2C MXenes.[32,33] The former exhibited paramagnetic behavior while the latter showed superconductivity-like diamagnetism. This limitation currently restricts their use in spintronics[34] and related fields.[35] Two strategies have emerged to address this issue: incorporating magnetic transition metal elements such as Co, Cr, Mn, Ni, V, and Fe,[36–41] or decorating MXenes with magnetic nanoparticles-an approach validated by numerous studies.

Tan *et al.*[42] synthesized $Ti_3C_2T_x$ MXene from carbon soot extracted from fossil fuel combustion waste and decorated it with Fe_3O_4 *via* hydrothermal treatment for vanadium redox flow batteries. Similarly, iron oxide nanodots were self-assembled on MXene surfaces for energy storage applications.[43] Hydrothermal methods have been widely employed to fabricate Fe_3O_4-based MXene composites for applications including photocatalysis,[44,45] electrochemical sensing,[46] and pollutant adsorption.[47,48] Zhang and co-workers[49] introduced hierarchical pore structures in MXene/Fe_3O_4/polyimide aerogels through directional freezing and thermal annealing for electromagnetic

[a]*Institute of Chemistry, Slovak Academy of Sciences, Dubravska cesta 5807/9, 845 38, Bratislava, Slovak Republic. E-mail: Jan.Tkac@savba.sk*
[b]*Department of Physical Chemistry and Theoretical Chemistry, Faculty of Natural Sciences, Comenius University, Mlynska dolina, 842 15, Bratislava, Slovak Republic*
[c]*International Laser Centre-Slovak Centre of Scientific and Technical Information, Ilkovicova 3, 841 04, Bratislava, Slovak Republic*
[d]*Department of Plasma Physics and Technology, CEPLANT—R&D Centre for Plasma and Nanotechnology Surface Modifications, Faculty of Science, Masaryk University, Kotlářská 267/2, 602 00 Brno, Czech Republic*
[e]*Institute of Materials and Machine Mechanics, Dubravska cesta 9/6319, 845 13, Bratislava, Slovak Republic*
[f]*Center for Advanced Materials, Qatar University, P.O. Box 2713, Doha, Qatar*
[g]*Department of Analytical Chemistry, Faculty of Natural Sciences, Comenius University, Ilkovicova 6, 842 15 Bratislava, Slovak Republic*
[h]*RCQI, Institute of Physics, Slovak Academy of Sciences, Dubravska cesta 9, 841 04, Bratislava, Slovak Republic*
[i]*Qatar Environment and Energy Research Institute, Hamad Bin Khalifa University, P.O. Box 34110, Doha, Qatar*

interference (EMI) shielding. Various fabrication approaches-including layer-by-layer assembly,[50,51] electrospinning,[52] hydrothermal synthesis,[53–55] and precipitation methods[56,57]-have been utilized to develop magnetic MXene hybrids for EMI shielding applications. The dielectric-magnetic synergistic effect for effective electromagnetic wave absorption was demonstrated in MXene/Fe_3O_4@Fe_3C@carbon composites.[55] Other notable applications include tannic acid-Fe_3O_4@MXene hydrogels with advanced conductivity and flexibility,[58] multichamber Fe_3O_4/$Ti_3C_2T_x$@rGO structures for broadband microwave absorption,[59] Fe_3O_4@$Ti_3C_2T_x$ composites for antibiotic degradation,[60] covalently bonded Fe_3O_4-MXene hybrids for microwave absorption,[61] and gradient-structured cellulose/MXene/Fe_3O_4 films for EMI shielding.[51] Magnetic N-TiO_2/Fe_3O_4@MXene showed high photo-Fenton degradation capacity for phenol,[62] while magnetically recyclable Fe_3O_4/Ti_3C_2 composites were developed for tetracycline adsorption.[63] Hierarchically porous Fe_3O_4/SiO_2/MXene/rGO[64] and Fe_3O_4/MoS_2/MXene[65] aerogels were prepared for microwave absorption. Magnetically enhanced photothermal antibacterial activity was observed for Fe_3O_4 grown *in situ* on MXene nanosheets with polydopamine coating.[66] Additionally, sandwich-type electrochemical biosensors based on Fe_3O_4–NH_2 and Ti_3C_2 MXene were developed for exosome detection with high sensitivity.[67]

Most preparation methods involve at least a two-step procedure: separate synthesis of MXenes and nanoparticles, followed by their combination to obtain hybrid composites. In this work, we demonstrate that benchmark MXenes—Ti_3C_2, Nb_4C_3, and Nb_2C—can be directly decorated *in situ* with magnetic nanoparticles fabricated *via* laser ablation in liquid (LAL).[68] To our knowledge, only one report describes LAL-mediated Fe nanocluster formation on $Ti_3C_2T_x$ for ammonia sensing.[69] LAL enables production of colloidally stable, ligand-free nanoparticles with tunable surface chemistry under ambient conditions.[70,71] Nanoparticles produced by LAL exhibit surface defects providing electrostatic stabilization, and the absence of surface ligands results in enhanced catalytic performance compared to chemically synthesized nanoparticles.[70]

Here we propose synthesis of iron oxide (Fe_yO_z) nanoclusters on three types of MXenes ($Ti_3C_2T_x$, Nb_2CT_x and $Nb_4C_3T_x$). We characterized the resulting magnetic nanocomposites by applying scanning electron microscopy (SEM), secondary ion mass spectrometry (SIMS), X-ray photoelectron spectroscopy (XPS), electrochemical performance in a plain buffer and an optical Faraday effect. We also investigated performance of hybrid nanocomposites for the reduction of H_2O_2.

Materials and methods

Reagents and materials

The phosphate buffer (PB) components (*i.e.* KH_2PO_4 and K_2HPO_4, pH 7.0), dimethyl sulfoxide (DMSO) were of ≥99% purity or p.a. grade and were purchased from Sigma-Aldrich (USA). 50% aq. HF was purchased from Fisher chemicals. The PB solution was freshly prepared in 0.055 μS ultrapure deionized water (DW). DW was obtained from Milli-Q® HX 7000 SD all-in-one system.

Synthesis of $Ti_3C_2T_x$, $Nb_4C_3T_x$ and Nb_2CT_x MXenes

$Ti_3C_2T_x$ MXene was prepared by selective Al etching by *in situ*-formed HF (reaction of LiF with HCl) using a previously described protocol.[72] The multilayered (ML) $Nb_4C_3T_x$ and Nb_2CT_x MXenes were prepared by selective Al etching from Nb_4AlC_3 and Nb_2AlC MAX phase, respectively, by hydrofluoric acid (HF) to remove Al layer as it was previously reported.[73,74] The stirred dispersions of Nb_2AlC or Nb_4AlC_3 powders immersed in 50% HF aqueous solution were heated at temperature of 40 °C for 96 h. After cooling, the resulted dispersion was thoroughly washed by DW six times and separated by centrifugation at 3500 rpm to obtain the multilayered-MXenes (ML-MXenes) as remaining residue from the supernatants. The ML-MXenes were finally washed using ethanol, and dried at 30 °C under argon atmosphere.

The subsequent delamination of ML-$Nb_4C_3T_x$ was performed by intercalation and ultrasonic treatment at 60% amplitude using 750 W by Hielscher Ultrasonics instrument. The dispersion of ML-$Nb_4C_3T_x$ (500 mg) in DMSO (10 mL) was stirred for 24 h. Then the residue was isolated by centrifugation followed by decantation of the supernatant. Finally, the delaminated product (DL) $Nb_4C_3T_x$ was achieved by probe sonication (Hielscher Ultrasonics instrument)[75] of dispersion of ML-$Nb_4C_3T_x$ (20 mg mL^{-1}) in DW at 20 °C in Ar atmosphere for 1 h. ML-Nb_2C MXene was similarly processed. The resulting solution was centrifuged at 5000 rpm for 10 min and decanted followed by freeze drying to get delaminated Nb_2CT_x or $Nb_4C_3T_x$ nanosheets (DL-Nb_2CT_x or DL-$Nb_4C_3T_x$).

Preparation of MXene@Iron oxide nanoparticle composites by laser ablation in liquid

An amplified Ti:Sapphire system (COHERENT Legend DUO) produced pulse trains with a repetition rate of 3 kHz at central wavelength of 800 nm and with pulse energies of 2.7 mJ at 120 fs. The beam was routed to a cuvette containing 1 mL of the dispersion (deionized water + MXene) and focused by a lens with a focal length of 175 mm onto the Fe target (purchased from Goodfellow Cambridge Ltd.) immersed 1 mm below the surface of the dispersion. The peak laser density at the focus was thus on the order of 10^{14} W cm^{-2}. The Fe target was exposed to laser radiation for 30 s. Thus, the laser ablation in liquid proceeded at a rate of 3000 pulses per s. Note that we were dynamically removing water vapor from above the cuvette and thus improving the laser beam coupling onto target. The as prepared MXenes patterned by Fe oxides (Fe_yO_z) nanoparticles (FeNPs) were carefully centrifuged and rinsed three times with deionized water to remove the unattached iron particles composites and to obtain stable nanocomposites (MXene@FeNPs).

Instrumentation for characterization of MXenes and MXenes@Fe oxides nanoparticle composites

Scanning electron microscopy (SEM). The surface morphology and chemical composition of synthesized $Ti_3C_2T_x$, $Nb_4C_3T_x$ and Nb_2CT_x MXenes and their composites were

studied using a scanning electron microscope (JEOL JSM-7600F equipped with energy dispersive X-ray spectrometer, EDS from Oxford Instruments X-Max 50 mm^2). Energy dispersive spectroscopy (EDS) was used to analyze the chemical composition with INCA analysis software. All SEM-EDS measurements were performed at an operating voltage of 15 kV with a 70 nm aperture. The standardized magnesium reference was used as the calibration element for optimization of chemical composition measurements.

Secondary ion mass spectrometry (SIMS). Secondary ion mass spectrometry (SIMS)[76,77] analysis was performed using a TOF-SIMS IV (ION-TOF, Muenster, Germany), a reflectron type of Time-of-Flight (TOF) mass spectrometer equipped with a Bi ion source providing data with a high sensitivity on the level of ppm–ppb. Pulsed 25 keV Bi^+ were used as primary ions with ion current of 1.1 pA. SIMS experiments were performed in both positive and negative polarity with details provided in our previously published works.

X-ray photoelectron spectroscopy (XPS). XPS measurements were carried out on an ESCALAB 250Xi X-ray Photoelectron Spectrometer (Thermo Fisher Scientific) at a take-off angle of 90°. The system is equipped with a 500-mm Rowland circle monochromator with a microfocused Al Kα X-ray source. An X-ray beam with a power of 200 W (650 μm spot size) was used. The survey spectra were acquired with a pass energy of 50 eV and an energy step of 1 eV. High-resolution Fe 2p scans were acquired with a pass energy of 20 eV and an energy step of 0.1 eV. The base pressure in the analysis chamber was in the 10^{-9} mbar range. An electron flood gun was used to compensate for the charge accumulation on the surface. Data calibration, processing, and fitting were performed with Avantage software.

Electrochemical behaviour. The laboratory potentiostat/galvanostat Autolab PGSTAT302N with an impedimetric module (Ecochemie, Utrecht, The Netherlands) was employed to study electrochemical performance of MXenes and MXene composites. The three-electrode cell system consisting of glassy carbon working electrode (GCE, $d = 3$ mm) used as a working electrode), an Ag/AgCl/3 M KCl reference electrode and a counter Pt electrode (Bioanalytical systems, USA) was applied. The surface area of GCE was pretreated and aqueous dispersions of MXenes (3 mg mL^{-1}) were prepared, as we mentioned in our previous study.[76] All electrochemical measurements were run under Nova Software 1.10, and data acquired were evaluated using OriginPro 9.1.

Optical Faraday effect. Our approach closely follows already published approach.[78,79] A 640 nm laser diode module (CPS635, THORLABS) was used as the light source. The beam passed through a Glan-Taylor polarizer (GT-10, THORLABS) and subsequently through the core of a solenoid. Here the beam passed through a glass cuvette filled with the sample solution. The polarization state has been resolved by passing the beam through a combination of a Wolaston polarizer (WP10, THORLABS) and a balanced detector (modified PDB210A, THORLABS). The output from the detector was coupled to a lock-in amplifier (SRS830, Stanford Research Systems). We have sampled the response at the fundamental (153 Hz) and third-harmonic frequency (459 Hz). The solenoid was driven by the trigger output of the lock-in amplifier coupled to a power amplifier through a series capacitance and hence by observing the RC resonant condition (at 153 Hz). The in-core magnetic field was calibrated by means of a Teslameter (GS-100D2). We have been working at low magnetic fields in order to limit the thermal loads on the coil.

Note that at the applied MXene concentrations, scattering was severely limiting our measurements as the MXene fraction would quickly sediment to the bottom of the cuvette thus creating a concentration gradient. Hence, we have applied a following protocol. After each measurement, the sample was taken out of the solenoid core and inserted into a shaker for 1 min and subsequently reinserted into the core. As the typical measurement only takes a couple of seconds, this approach allowed us to obtain consistent results.

Results and discussion

Microscopic characterization

The SEM imaging was performed on pristine samples of $Ti_3C_2T_x$, $Nb_4C_3T_x$ and Nb_2CT_x MXenes and subsequently on the *in situ* decorated samples (Fig. 1). The complex, multilayered structure of pristine $Ti_3C_2T_x$, $Nb_4C_3T_x$ and Nb_2CT_x MXenes is shown in Fig. 1a, c and e. As confirmed by Fig. 1b, d and f all three samples had shown substantial coverage by iron oxide (Fe_yO_z) nanoparticles (FeNPs), thereby proving our approach. Moreover, we have evaluated the NP size distribution and obtained median diameters of 65 nm, 85 nm and 115 nm for $Ti_3C_2T_x$, $Nb_4C_3T_x$, Nb_2CT_x, respectively (see SI, Fig. S1–S3) and

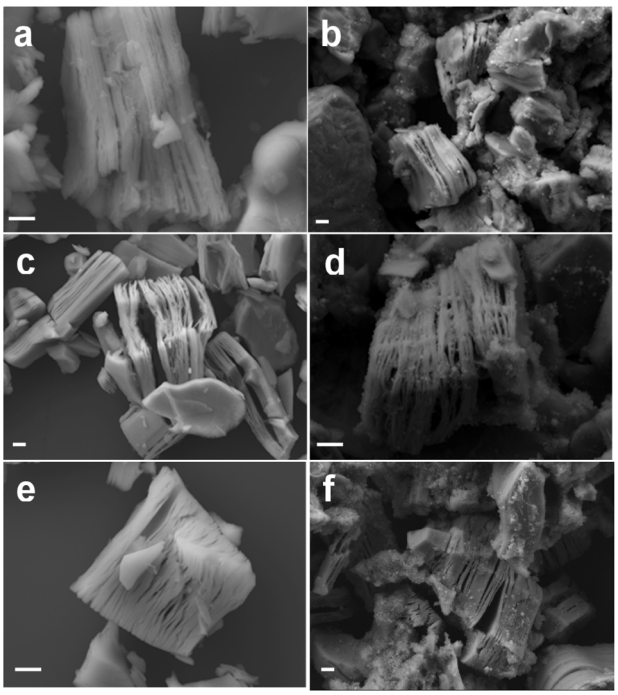

Fig. 1 Scanning electron micrographs showing the multilayered structure of MXenes, *i.e.* $Ti_3C_2T_x$ (a), $Nb_4C_3T_x$ (c), Nb_2CT_x (e) and MXene@FeNPs composites, *i.e.* $Ti_3C_2T_x$@FeNPs (b), $Nb_4C_3T_x$@FeNPs (d), Nb_2CT_x@FeNPs (f). The scale bar corresponds to 1 μm.

a relatively broad distribution function characteristic of LAL.[68] The 2D structure of MXenes was still preserved, after the nanocomposites were formed.

Secondary ion mass spectrometry characterization

The characteristic ions and molecules identified in the samples of $Ti_3C_2T_x$, $Nb_4C_3T_x$ and Nb_2CT_x MXenes and MXenes@FeNPs composites were obtained in the form of mass spectra in both positive and negative polarities. Fig. S2, S4, S6, S8, S10 and S12 show the mass spectra in a positive polarity and the identified ions and fragments with the corresponding isotopic distribution for MXenes and MXenes@FeNPs composites. Fig. S3, S5, S7, S9, S11 and S13 show the mass spectra in a negative polarity with identified ions and fragments originating from MXenes and MXenes@FeNPs composites molecules, as well as the iron oxide NPs themselves. SIMS spectra show a plethora of iron oxides, including FeO^+, Fe_2O^+, $Fe_3O_2^+$, $Fe_3O_3^+$.

SIMS 2D distributions for the selected fragments of $Ti_3C_2T_x$@FeNPs, $Nb_4C_3T_x$@FeNPs and Nb_2CT_x@FeNPs composites in both polarities are shown in Fig. 2 and 3, and additional data is shown in the supplementary information file, Fig. S14–S19. Time-of-Flight-SIMS imaging was performed to evaluate the lateral distribution of Fe species. The 2D SIMS images show a clear spatial correlation between the transition metal signal (Ti^+/Nb^+) and characteristic Fe oxide fragments (*e.g.*, FeO^+, Fe_2O^+, $Fe_3O_3^+$). The images were recorded over area of 250 × 250 μm.

Fig. 2, upper row represents the 2D distribution of the selected species in positive polarity: Ti^+, Fe^+ and the sum of FeO^+, $FeOH^+$, Fe_2O^+, $Fe_3O_2^+$, $Fe_3O_3^+$, $Fe_3O_3H^+$ and $Fe_3O_4H^+$ for $Ti_3C_2T_x$ MXene@FeNPs. Fig. 2, middle row represents the 2D distribution of the selected species in positive polarity: Nb^+, Fe^+ and the sum of Fe_2O^+, $Fe_3O_3^+$ for $Nb_4C_3T_x$ MXene@FeNPs. Fig. 2, lower row represents the 2D distribution of the selected species in positive polarity: Nb^+, Fe_+ and sum of FeO^+, $FeOH^+$, Fe_3O^+, $Fe_3O_2^+$, $Fe_3O_2^+$, $Fe_3O_3^+$, $Fe_3O_3H^+$ for Nb_2CT_x MXene@FeNPs.

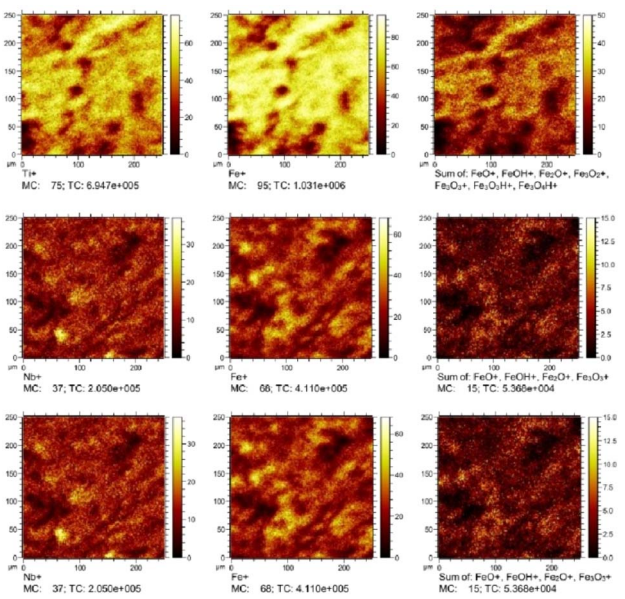

Fig. 2 SIMS 2D distribution for the selected fragments of $Ti_3C_2T_x$@FeNPs (upper row), $Nb_4C_3T_x$@FeNPs (middle row), Nb_2CT_x@FeNPs (lower row) in positive polarity.

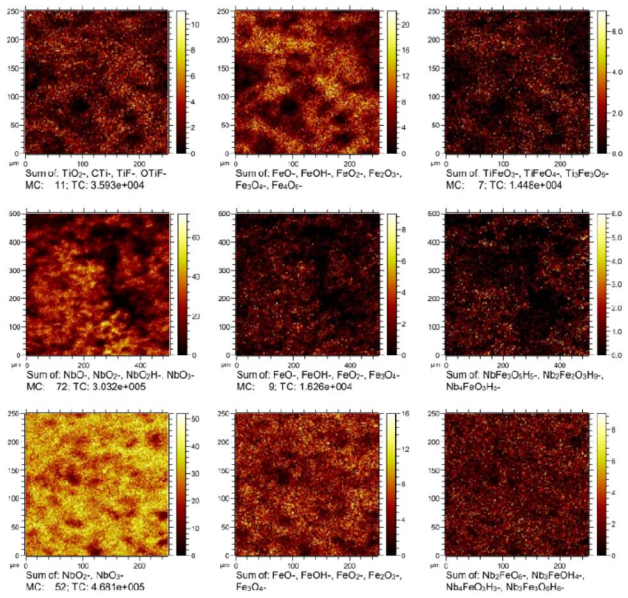

Fig. 3 SIMS 2D distribution for the selected fragments of $Ti_3C_2T_x$@FeNPs (upper row), $Nb_4C_3T_x$@FeNPs (middle row), Nb_2CT_x@FeNPs (lower row) in negative polarity.

Fig. 3, upper row represents the 2D distribution of the selected species in negative polarity: sum of TiO_2^-, CTi^-, TiF^- and $OTiF^-$, sum of FeO^-, $FeOH^-$, FeO_2^-, $Fe_2O_3^-$, $Fe_3O_4^-$ and $Fe_4O_6^-$ and sum of $TiFeO_3^-$, $TiFeO_4^-$ and $Ti_3Fe_3O_5^-$ for $Ti_3C_2T_x$ MXene@FeNPs. Fig. 3, middle row represents the 2D distribution of the selected species in negative polarity: sum of NbO^-, NbO_2^-, NbO_2H^- and NbO_3^-, sum of FeO^-, $FeOH^-$, FeO_2^- and $Fe_3O_4^-$ and sum of $NbFe_3O_5H_5^-$, $Nb_2Fe_2O_3H_9^-$ and $Nb_4FeO_3H_3^-$ for $Nb_4C_3T_x$ MXene@FeNPs. Fig. 3, lower row represents the 2D distribution of the selected species in negative polarity: sum of NbO_2^- and NbO_3^-, sum of FeO^-, $FeOH^-$, FeO_2^-, $Fe_2O_3^-$ and $Fe_3O_4^-$ and sum of $Nb_2FeO_6^-$, $Nb_3FeOH_4^-$, $Nb_4FeO_3H_3^-$ and $Nb_3Fe_3O_6H_6^-$ for Nb_2CT_x MXene@FeNPs. Unlike in positive polarity, we were also able to identify the $M_xFe_yO_z$ cluster ions.

The values of normalized intensities for identified ions in $Ti_3C_2T_x$, $Nb_4C_3T_x$ and Nb_2CT_x MXenes with iron oxide nanoparticles in positive and negative polarity are summarized in Table S1.

In summary, the SIMS imaging shows a clear correlation between the distribution of the respective transition metal and the characteristic iron cations. Hence, it can be concluded that the original terminations at the transition metal site of the parent MXene are now predominantly occupied by the iron oxide nanoparticles. This can be understood in terms of MXenes possessing surface terminations such as oxygen (O), hydroxyl (OH), and fluorine (F) inherited from their synthesis

from MAX phases and these further act as primary binding sites.[80,81] For instance, it has been shown that hydroxyl groups provide activated Ti sites that can strongly interact with metal ions (like Zn^{2+}).[82]

X-ray photoelectron spectroscopy (XPS) analysis

The formation of Fe nanoparticles (NPs) was further confirmed by XPS, a powerful surface-sensitive technique capable of identifying both elemental composition and oxidation states. As shown in Table 1, XPS analysis confirmed that the LAL method successfully produced MXenes enriched with Fe NPs. The highest efficiency was observed for Ti_3C_2, yielding a solution containing 15% Fe, of which 9% remained after water rinsing. For Nb_2C and Nb_4C_3 MXenes, the initial Fe NP contents were 9% and 5%, respectively, decreasing to 8% and 3% after rinsing.

High-resolution XPS spectra were used to determine the Fe^{2+}/Fe^{3+} ratios in the metal oxides.[83] Deconvolution of the Fe $2p_{3/2}$ peak revealed two main components: one at a binding energy (BE) of 710.9 eV corresponding to Fe^{2+}, and another at 713.4 eV representing Fe^{3+} (Fig. 4). Relative areas of these components are summarized in Table 1. A satellite peak located 7.9 eV higher than the main Fe $2p_{3/2}$ peak was also observed, providing a clear evidence for the presence of Fe^{2+}, since Fe^{3+} does not exhibit a satellite peak. The relative fractions of Fe_3O_4, FeO, and Fe_2O_3 were estimated from the deconvoluted Fe $2p_{3/2}$ spectra by quantifying Fe^{2+} and Fe^{3+} contributions (Table 1). This calculation assumed that all Fe is present exclusively in these three stoichiometric oxides. This assumption is supported by previous studies, which indicate that the LAL method frequently produces mixed FeO, Fe_2O_3, and Fe_3O_4.[84–86] Stoichiometric Fe_3O_4 can also be written as $FeO{\cdot}Fe_2O_3$; therefore, the Fe^{2+}/Fe^{3+} ratio was set to 1 : 2 (FeO contains only Fe^{2+}, whereas Fe_2O_3 contains only Fe^{3+}). A set of linear equations was established to relate the experimentally determined Fe^{2+}/Fe^{3+} ratio to the contributions from each oxide phase. Solving these equations yielded the relative phase composition, providing a straightforward means of estimating the oxide distribution directly from XPS measurements.[83]

Table 1 Relative fractions of Fe_3O_4, FeO, and Fe_2O_3 derived from Fe^{2+}/Fe^{3+} ratios obtained by XPS for Fe-dopped MXenes (Ti_3C_2, Nb_2C, Nb_4C_3). The data highlight the influence of MXene type and rinsing on Fe oxide phase stability

	Ti_3C		Nb_2C		Nb_4C_3	
	Non-rinsed	Rinsed	Non-rinsed	Rinsed	Non-rinsed	Rinsed
Fe (at%)	14.9 ± 0.7	8.6 ± 1.8	8.9 ± 0.3	7.9 ± 0.4	5.3 ± 0.2	3.1 ± 0.1
Fe^{2+}	59 ± 2	53 ± 1	57 ± 2	62 ± 1	53 ± 1	70 ± 2
Fe^{3+}	41 ± 2	47 ± 1	43 ± 2	38 ± 1	47 ± 1	30 ± 2
Fe_3O_4	50	50	50	50	55	30
FeO	42	36	40	45	35	60
Fe_2O_3	8	14	10	5	10	10

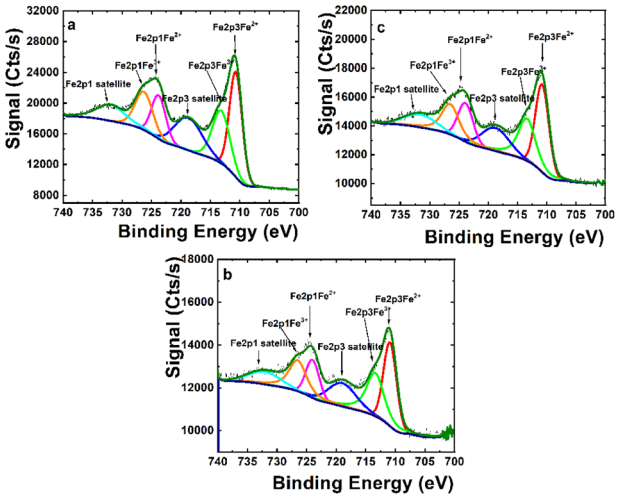

Fig. 4 High-resolution Fe 2p XPS spectra of $Ti_3C_2T_x$@FeNPs (a), $Nb_4C_3T_x$@FeNPs (b) and Nb_2CT_x@FeNPs (c).

For Ti_3C_2 and Nb_2C, Fe_3O_4 constitutes 50% of the total Fe oxides regardless of rinsing, indicating high stability of the mixed-valence phase. In Ti_3C_2, rinsing decreases FeO (from 42% to 36%) while increasing Fe_2O_3 (from 8% to 14%), suggesting partial oxidation of Fe^{2+} to Fe^{3+}. Conversely, Nb_2C exhibits a slight increase in FeO (from 40% to 45%) and a decrease in Fe_2O_3 upon rinsing, implying enhanced stabilization of Fe^{2+} species. For Nb_4C_3, however, a more pronounced change is observed. The Fe oxide distribution shifts from Fe_3O_4 = 55%, FeO = 35%, and Fe_2O_3 = 10% in the non-rinsed sample to Fe_3O_4 = 30%, FeO = 60%, and Fe_2O_3 = 10% after rinsing. The overall Fe content simultaneously decreases from 5 at% to 3 at%, indicating that rinsing leads primarily to the removal of weakly bound Fe_3O_4 nanoparticles rather than to chemical transformation of Fe species. The apparent increase in the Fe^{2+}/Fe^{3+} ratio (70/30) also reflects the preferential leaching of Fe^{3+}-containing phases.

These observations demonstrate that Fe oxide stability on MXene surfaces is composition-dependent. Ti_3C_2 and Nb_2C retain nearly constant oxide distributions upon rinsing, confirming strong surface adhesion and chemical stability of the deposited Fe phases. In contrast, Nb_4C_3 shows partial loss of Fe_3O_4 during rinsing, suggesting that, Fe nanoparticles are more weakly anchored to this substrate and more susceptible to removal in aqueous media.

Presence of three different types of Fe oxides on MXene *i.e.* magnetite (Fe_3O_4), Fe_2O_3 and FeO generated from Fe target using LAL is in an excellent agreement with the literature.[87]

Based on SIMS analysis, the Fe-related species are distributed across the analysed surface without evidence of macroscopic segregation or localized clustering. These results indicate that Fe oxide nanoparticles are laterally distributed over the MXene surface at the micrometer scale. Although minor nanoscale variations cannot be excluded, the combined XPS and ToF-SIMS results demonstrate that the Fe loading is

sufficiently homogeneous for reliable catalytic performance evaluation.

Electrochemical performance of pristine MXenes and MXene-based Fe nanocomposites

All types of MXenes exhibit a significant anodic peak, which decreases with a number of scans during CVs (Fig. 5b, d and f). While an anodic peak for $Ti_3C_2T_x$ appears at a potential of 367 mV (Fig. 5b), for Nb_2CT_x it appears at a potential of 545 mV (Fig. 5d) and for $Nb_4C_3T_x$ at a potential of 479 mV (Fig. 5f). Thus, while for oxidation of $Ti_3C_2T_x$ the lowest potential is required for its oxidation such MXene material is the least electrochemically/redox stable. On the other hand, the highest potential of 545 mV was required for the oxidation of Nb_2CT_x; thus, Nb_2CT_x is the most electrochemically/redox-stable MXene among those investigated in the study, with $Nb_4C_3T_x$ MXene being moderately stable. Electrochemical/redox stability in the order Nb_2CT_x > $Nb_4C_3T_x$ > $Ti_3C_2T_x$ is also confirmed by the kinetics of MXene oxidation with increasing number of scans, as shown in Fig. 6a.

Interestingly, the Nb_2CT_x MXene exhibits rather wide oxidation peak, most likely due to two different redox processes at a potential of ~310 mV and 545 mV (the main or maximal peak) (Fig. 5d), suggesting a more complex redox/electrochemical behaviour of Nb_2CT_x compared to $Nb_4C_3T_x$ and $Ti_3C_2T_x$ MXenes.

A decrease of an anodic peak with a number of scans during CVs was well described for $Ti_3C_2T_x$ MXene[76] and was attributed

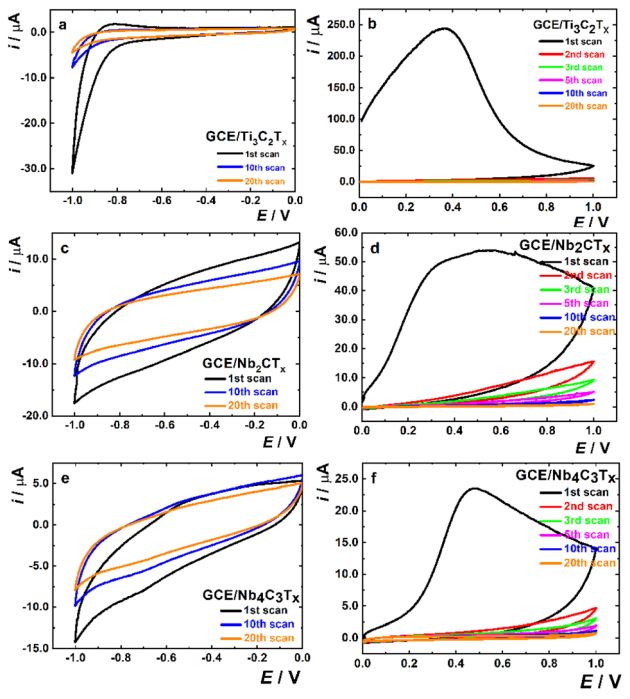

Fig. 5 Electrochemical performance of $Ti_3C_2T_x$, Nb_2CT_x, and $Nb_4C_3T_x$ MXenes at negative (a, c and e) or positive potentials (b, d and f). CVs were run in 0.1 M PB pH 7.0 at a sweep rate of 100 mV s^{-1} with 20 scans collected. Anodic (plasmon) peaks are visible for all three MXenes *i.e.* $Ti_3C_2T_x$ (b); Nb_2CT_x (d) and $Nb_4C_3T_x$ (f).

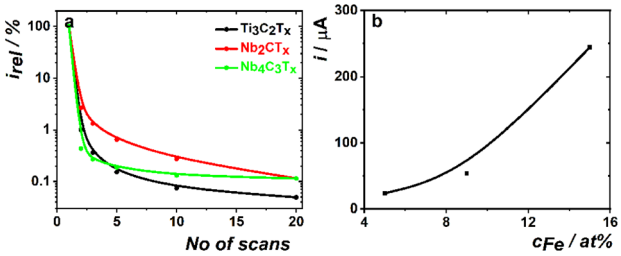

Fig. 6 Stability of an anodic peak current (*i.e.* the highest anodic peak due to presence of surface plasmons) for $Ti_3C_2T_x$ (current read at 367 mV), Nb_2CT_x (current read at 545 mV), and $Nb_4C_3T_x$ (current read at 479 mV) MXenes during several cycles in CVs run in 0.1 M PB pH 7.0 at a sweep rate of 100 mV s^{-1} (a). Correlation between the content of Fe within the MXene-based nanocomposites and an anodic (plasmon) peak current observed in the 1st scan of CVs (Fig. 5b, d and e) using all types of MXenes (b).

to the presence of plasmons *i.e.* presence of free electrons and upon oxidation of $Ti_3C_2T_x$ MXene, such plasmons are channels to the electrode, resulting in oxidized $Ti_3C_2T_x$ MXene with significantly altered electrochemical performance.[76] Thus, Nb_2CT_x and $Nb_4C_3T_x$ MXenes should not be exposed to conditions exceeding such an oxidation potential in order to not significantly alter electrochemical/redox performance of Nb-based MXenes, similarly to the case of $Ti_3C_2T_x$ MXene. Decrease of an anodic peak for Nb_2CT_x and $Nb_4C_3T_x$ MXenes was also described recently.[88]

All of the explored MXenes have metallic like bands at E_F with large density of states that is due to Ti 3d bands in $Ti_3C_2T_x$ and Nb 4d bands in the Nb based MXenes. Under normal conditions, they would all support collective electron oscillations and hence plasmons with the plasmon strength given by the following order: $Nb_4C_3T_x$ > Nb_2CT_x > $Ti_3C_2T_x$. However, under strong oxygen and hydroxyl termination the order can be fully reversed. *i.e.* $Ti_3C_2T_x$ > Nb_2CT_x > $Nb_4C_3T_x$. We are arguing this is indeed the case due to the following: (1) the order given by the plasmon response as identified from Fig. 5d, e and f and (2) SIMS data, specifically the images S18, S19 and Table S2.

It is worth mentioning that the electrochemical behavior of all types of MXenes is more stable in the cathodic potential window (Fig. 5a, c and e), with Nb-based MXenes being more stable compared to $Ti_3C_2T_x$ MXene.

The redox/electrochemical behavior of $Nb_4C_3T_x$ MXene in the cathodic potential window with a cathodic peak at ~−700 mV and an anodic peak at a potential of ~−530 mV (Fig. 5e) is in an excellent agreement with published data *i.e.* peaks at −700 mV or −490 mV, respectively, for $Nb_3C_4T_x$ MXene.[89] Two redox peaks at approximately the same potential were present on Nb_2CT_x (Fig. 5c), but more hidden in the capacitive currents.

Since the current of an anodic (plasmon) peak represents density of plasmons present in MXenes it is reasonable to assume that the density of free electrons (plasmons) can have a detrimental effect on the Fe loading capacity on MXenes during LAL process. The rationale behind is electrostatic attraction of positively charged Fe cations generated during LAL process and negatively charged MXenes. We found that the

current intensity of anodic (plasmon) peak observed on pristine MXenes is increasing with an increasing the amount of Fe species deposited on MXenes during formation of MXene nanocomposites (Fig. 6b). Thus, we can conclude that the density of free electrons (plasmons) within the pristine MXenes affects effectivity of Fe deposition during LAL on pristine MXenes and thus also Fe surface coverage on the MXene nanocomposites.

Although, plasmon density expressed as anodic (plasmon) peak current is significantly lower on Nb_2CT_x and $Nb_4C_3T_x$ MXenes, it can be effectively enhanced by the procedure of MXene synthesis from MAX phases. In the past we showed that density of plasmons expressed as anodic (plasmon) peak current was significantly lower on to $Ti_3C_2T_x$ MXene when prepared using HF etching compared to LiF + HCl etching.[90] Since Nb_2CT_x and $Nb_4C_3T_x$ MXenes in this study were prepared by HF etching from their MAX phases, altered synthesis of Nb_2CT_x and $Nb_4C_3T_x$ MXenes from their MAX phases (*i.e.* using LiF + HCl etchants) can enhance density of plasmons within Nb_2CT_x and $Nb_4C_3T_x$ MXenes and thus also efficiency of Fe deposition on Nb_2CT_x and $Nb_4C_3T_x$ MXenes using LAL.

It is noteworthy, that of an anodic peak at +550 mV on all nanocomposite electrodes (Fig. 7a, c and e), *i.e.* in an agreement for redox potential of $Fe^{2+/}Fe^{3+}$ redox couple (770 mV *vs.* NHE *i.e.* 570 mV *vs.* Ag/AgCl).[91] Thus, we can attribute this peak to the redox/electrochemical activity of Fe species deposited on MXenes during LAL process. We were tempted to correlate the peak current observed at +550 mV on the nanocomposites with the electrochemical ability of nanocomposites to electrochemically reduce hydrogen peroxide by the electrochemically active Fe species present on the nanocomposites. When the peak current observed at +550 mV on nanocomposites was correlated to current observed for H_2O_2 reduction using nanocomposites (*i.e.* read at potential of −1000 mV) a good correlation was observed with $R^2 = 0.990$ (Fig. 8). Thus, the intensity of the peak at 550 mV can be attributed to the density of electrochemically active Fe species responsible for H_2O_2 reduction.

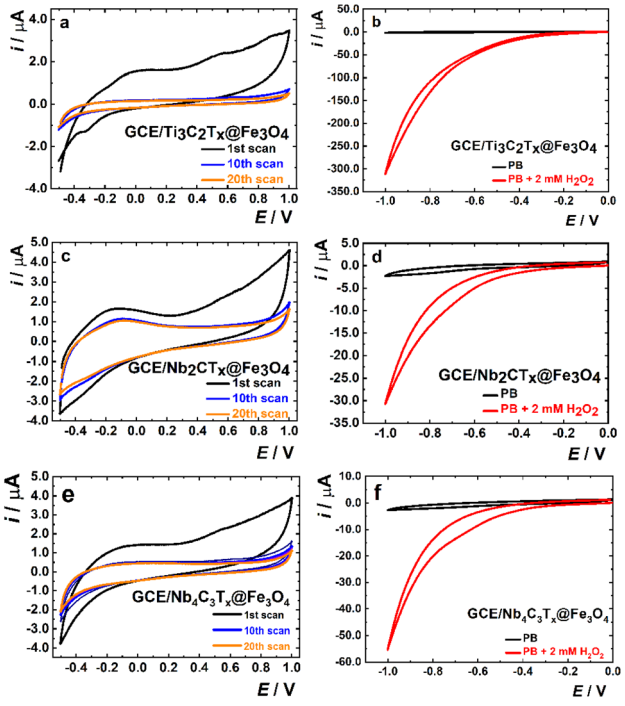

Fig. 7 Electrochemical behaviour of $Ti_3C_2T_x$, Nb_2CT_x, and $Nb_4C_3T_x$ MXene-based nanocomposites with deposited Fe species in 0.1 PB pH 7.0 run at a sweep rate of 100 mV s^{-1} (a, c and e). Electrochemical ability of $Ti_3C_2T_x$, Nb_2CT_x, and $Nb_4C_3T_x$ MXene-based nanocomposites with deposited Fe species to reduce hydrogen peroxide run in 0.1 PB pH 7.0 run at a sweep rate of 100 mV s^{-1} (b, d and f).

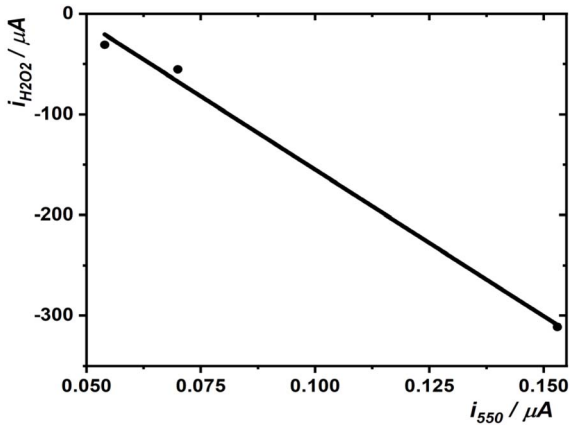

Fig. 8 Correlation between the electrocatalytic peak current observed for electrochemical reduction of hydrogen peroxide read at −1000 mV from Fig. 7b, d and f and an anodic peak observed at +550 mV on the nanocoposites (read from Fig. 7a, c and e) with $R^2 = 0.990$.

The peak currents obtained at three different MXene-based nanocomposites can be converted to current densities using geometric surface area of 7.1 mm^2 [90] as follows: 4399 μA cm^{-2} ($Ti_3C_2T_x$), 434 μA cm^{-2} (Nb_2CT_x) and 782 μA cm^{-2} ($Nb_3C_4T_x$). The value of current density of 4399 μA cm^{-2} for H_2O_2 reduction obtained using $Ti_3C_2T_x$ MXene-based nanocomposite is significantly higher compared to the value of current density of 2020 μA cm^{-2} for H_2O_2 reduction obtained using pristine $Ti_3C_2T_x$ MXene.[90] Thus, LAL deposition of Fe species on MXenes is a promising way to achieve highly electrochemically active nanocomposites for H_2O_2 reduction using non-precious metals. We assume that synthesis of Nb_2CT_x and $Nb_4C_3T_x$ MXenes using LiF + HCl synthetic route can enhance density of Fe species deposited on such MXenes and also increase density of electrochemically active Fe species, responsible for efficient H_2O_2 reduction.

Optical Faraday effect

Optical Faraday effect can be considered a benchmark technique for characterization of (optically) transparent magnetically active materials, see supplementary information, Fig. S20. Here, sample response at slowly alternating magnetic fields at a frequency of 153 Hz was observed. We started by exploring the Faraday response of LAL-prepared NP solutions in water with no MXenes added, see supplementary information, Fig. S21. They show a regular response well within the model described by

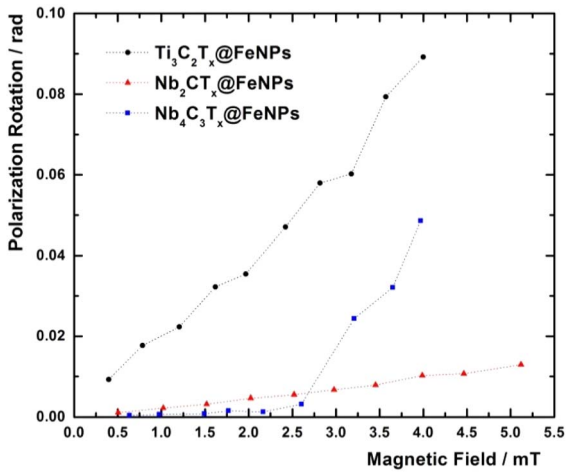

Fig. 9 Faraday optical response of the $Ti_3C_2T_x$@FeNPs, Nb_2CT_x@FeNPs, and $Nb_4C_3T_x$@FeNPs nanocomposites. The solid lines are only to guide an eye.

Patterson *et al.*[78] developed for characterization of superparamagnetic NPs.

Next, we have switched to sample solutions containing nanocomposites. The obtained Faraday response is depicted in Fig. 9. All three MXenes under study do show magnetic properties but none of them qualitatively resembles the response of pure NPs. Most strikingly, while the NP-decorated $Ti_3C_2T_x$ and Nb_2CT_x both show a monotonically rising Faraday response the $Nb_4C_3T_x$ shows an activated response with the polarization rotation angle being negligible up until approximately 2.2–2.5 mT after which we do observe a steep rise.

Also note that of the three MXenes under study the Ti_3C_2 exhibited the strongest Faraday response within the experimentally attainable range of 0–4 mT. Given the similar coverage of all three MXenes by NPs the difference cannot be simply explained by higher NP concentration for the given sample. Direct comparison between XPS data given in Table 1 and the Faraday response shows that, at low magnetic fields, up to approximately 2.5 mT, the signal magnitude for respective MXene samples follows the ordering given by either Fe or Fe_3O_4 content, *i.e.* $Ti_3C_2T_x \geq Nb_2CT_x > Nb_4C_3T_x$. Consequently, we may speculate that at low enough mag. fields, the response is still linear and representing the actual Fe loading, while at higher fields we are entering a nonlinear regime and a direct correspondence cannot be drawn anymore.

In fact, a quantitative modeling would be needed in order to get a deeper insight into observed phenomenology. Note that our main goal here was to prove that the composite system MXene + NPs would inherit/retain magnetic properties of the NPs and not to provide a thorough quantitative analysis.

Conclusions

We have introduced a novel method for synthesis of MXene-based Fe nanocomposites using LAL allowing to prepare Fe-based nanoclusters on the surface of MXenes without any ligands, which are needed during deposition of nanoclusters on surfaces using traditional ways. The coverage of Fe on the MXene surfaces varied in the range from 5 to 15 at% of Fe depending on MXene used for deposition. Interestingly we showed that the current of plasmon peak representing density of free plasmons observed on pristine MXenes is the main driving force besides deposition of Fe species on MXenes. Furthermore, we observed that the anodic peak at +550 mV on MXene-based Fe nanocomposites represent electrochemically active Fe species with intensity of such anodic peak at +550 mV in a direct correlation with electrochemical activity of MXene-based Fe nanocomposites towards H_2O_2 reduction. The highest current density of electrochemical reduction of H_2O_2 was observed on $Ti_3C_2T_x$ MXene-based Fe nanocomposite with a value of 4399 μA cm^{-2}. We also proposed that significantly higher electrochemical reduction of H_2O_2 could be observed also on Nb_2CT_x and $Nb_4C_3T_x$ MXene-based Fe nanocomposites, when using HF + HCl method for synthesis of MXenes from MAX phases. Furthermore, we have proven that the MXene-based Fe nanocomposites are magnetically active with potential to use them for some separation processes. Moreover, presence of plasmons within Nb_2CT_x and $Nb_4C_3T_x$ MXenes could be used for spontaneous grafting of (bio)molecules using diazonium grafting-based process as was described in our earlier work on $Ti_3C_2T_x$ MXene.[92] Finally, it may be of great merit to test MXene-based nanocomposites using different nanoclusters deposited on MXenes using LAL for other specific purposes such as glycan enrichment and such study are underway in our laboratories.[93]

Author contributions

Lenka Lorencová – writing – original draft, methodology, investigation, formal analysis, conceptualization. Eva Noskovičová – investigation. Monika Jerigová – investigation. Monika Stupavská – writing – original draft, investigation, formal analysis. Ľubomír Orovčík – investigation. Lucia Kopčanová – investigation. Peter Kasák – investigation. Andrej Vikartovský – investigation. Dušan Lorenc – investigation, writing – original draft. Khaled A. Mahmoudi – investigation. Ján Tkáč – writing – original draft, supervision.

Conflicts of interest

There are no conflicts to declare.

Data availability

The data supporting this article have been included as part of the supplementary information (SI) *i.e.* the file "Supporting information file – "raw data.xlsx". Supplementary information is available. See DOI: https://doi.org/10.1039/d6ra00426a.

Acknowledgements

The authors would like to acknowledge the financial support received from the projects of Slovak Research and Development

Agency (APVV-22-0345 and APVV-23-0083). This work was jointly supported by Qatar University and Institute of Chemistry, Slovak Academy of Sciences-IRCC-2024-429. The findings achieved herein are solely the responsibility of the authors. The work was funded by the EU NextGenerationEU through the Recovery and Resilience Plan for Slovakia under the project no. 09105-03-V02-00070. This research has been also supported by the project LM2023039 funded by the Ministry of Education, Youth and Sports of the Czech Republic.

References

1 M. Naguib, M. Kurtoglu, V. Presser, J. Lu, J. Niu, M. Heon, L. Hultman, Y. Gogotsi and M. Barsoum, Two-Dimensional Nanocrystals Produced by Exfoliation of Ti_3AlC_2, *Adv. Mater.*, 2011, **23**, 4248.

2 M. Naguib, V. Mochalin, M. Barsoum and Y. Gogotsi, 25th Anniversary Article: MXenes: A New Family of Two-Dimensional Materials, *Adv. Mater.*, 2014, **26**, 992.

3 L. Pandey, W. Liang, A. VahidMohammadi, T. Zhang, Y. Gogotsi and M. Wanunu, Hydrophilicity and Surface Charge Modulation of $Ti_3C_2T_x$ MXene Based Membranes for Water Desalination, *RSC Adv.*, 2024, **14**, 21635.

4 J. Simon, C. Fruhling, H. Kim, Y. Gogotsi and A. Boltasseva, MXenes for Optics and Photonics, *Opt. Photonics News*, 2023, **34**, 44.

5 P. Viviani, E. Gibertini, P. Fontana, F. Lissandrello, Y. Gogotsi and L. Magagnin, Flexible Inkjet-Printed Lithium-Ion Batteries with $Ti_3C_2T_x$ Current Collector, *J. Power Sources*, 2024, **601**, 234287.

6 N. Noriega, M. Shekhirev, C. Shuck, J. Salvage, A. VahidMohammadi, M. Dymond, J. Lacey, S. Sandeman, Y. Gogotsi and B. Patel, Pristine $Ti_3C_2T_x$ MXene Enables Flexible and Transparent Electrochemical Sensors, *ACS Appl. Mater. Interfaces*, 2024, **16**, 6569.

7 A. Inman, T. Parker, Y. Zhang, M. Saraf and Y. Gogotsi, Obtaining a Practical Wearable Supercapacitor Power Supply, *Adv. Energy Mater.*, 2024, **14**, 2402367.

8 F. Shahzad, M. Alhabeb, C. Hatter, B. Anasori, S. Hong, C. Koo and Y. Gogotsi, Electromagnetic Interference Shielding with 2D Transition Metal Carbides, in. *MXenes: from Discovery to Applications of Two-Dimensional Metal Carbides and Nitrides*, 2023, pp. 933–947.

9 J. Hu, N. Hu, D. Pan, Y. Zhu, X. Jin, S. Wu and Y. Lu, Smell Cancer by Machine Learning-Assisted Peptide/MXene Bioelectronic Array, *Biosens. Bioelectron.*, 2024, **262**, 116562.

10 S. Avinashi, R. Mishra, R. Singh, N. Shweta, N. Rakhi, Z. Fatima and C. Gautam, Fabrication Methods, Structural, Surface Morphology and Biomedical Applications of MXene: A Review, *ACS Appl. Mater. Interfaces*, 2024, **16**, 47003.

11 X. Lin, D. Song, T. Shao, T. Xue, W. Hu, W. Jiang, X. Zou and N. Liu, A Multifunctional Biosensor via MXene Assisted by Conductive Metal–Organic Framework for Healthcare Monitoring, *Adv. Funct. Mater.*, 2024, **34**, 2311637.

12 L. Lorencova, P. Kasak, N. Kosutova, M. Jerigova, E. Noskovicova, A. Vikartovska, M. Barath, P. Farkas and J. Tkac, MXene-Based Electrochemical Devices Applied for Healthcare Applications, *Microchim. Acta*, 2024, **191**, 88.

13 A. Vikartovský, N. Košútová, L. Lorencová, P. Kasák, T. Bertók and J. Tkáč, Cutting-Edge Aptasensing Approaches for Electrochemical Detection of Exosomes Utilizing MXenes, *Chemelectrochem*, 2025, **12**, e202400713.

14 J. Xiong, X. Zhao, Z. Liu, H. Chen, Q. Yan, H. Lian, Y. Chen, Q. Peng and X. He, Multifunctional Nacre-Like Nanocomposite Papers for Electromagnetic Interference Shielding via Heterocyclic Aramid/MXene Template-Assisted In-Situ Polypyrrole Assembly, *Nano-Micro Lett.*, 2025, **17**, 53.

15 Y. Li, Y. Wang, Z. Xu, B. Peng, N. Tran, K. Saxena, S. Vadivel and X. Liu, MXene-Based Materials for Efficient Applications in Perovskite Solar Cells: A Review, *J. Mater. Sci. Technol.*, 2025, **215**, 214.

16 D. Zhang, K. Hantanasirisakul & Y. Gogotsi, MXenes' Optical and Optoelectronic Properties and Related Applications, in. *Transition Metal Carbides and Nitrides (MXenes) Handbook: Synthesis, Processing, Properties and Applications*, 2024, pp. 429–452.

17 Y. Zhao, Z. Guan, Z. Wei, L. Fu, L. Chen, Z. Huang, M. Humphrey and C. Zhang, Enhanced Nonlinear Optical Properties of MXene ($Ti_3C_2T_x$) via Surface-Covalent Functionalization with Porphyrin, *Mater. Today Phys.*, 2024, **48**, 101577.

18 H. Zhang, C. Hao, T. Fu, D. Yu, J. Howe, K. Chen, N. Yan, H. Ren and H. Zhai, Gradient-Layered MXene/Hollow Lignin Nanospheres Architecture Design for Flexible and Stretchable Supercapacitors, *Nano-Micro Lett.*, 2025, **17**, 43.

19 X. Zhang, Y. Su, J. Xu, Y. Jin, H. Zhang, G. Ma, J. Xu, M. Zhou, X. Zhou, F. Cao, Y. Chang, Y. Wang, B. Zhao, S. Yi, J. Chen, D. Fang, X. Lv and L. Liu, Self-Adhesive ILn@MXene Multifunctional Hydrogel with Excellent Dispersibility for Human-Machine Interaction, Capacitor, Antibacterial and Detecting Various Physiological Electrical Signals in Humans and Animals, *Nano Energy*, 2025, **133**, 110484.

20 A. Amani, A. Rahbar, E. Vafa, L. Tayebi, M. Abbasi, H. Kamyab, S. Chelliapan, S. Kasaee, A. Vaez and S. Mosleh-Shirazi, Exploring the Functionality of MXenes as Promising Versatile Antimicrobial Agents and Their Novel Applications, *Mater. Today Commun.*, 2024, **41**, 110774.

21 X. Zhao, Y. Chen, R. Niu, Y. Tang, Y. Chen, H. Su, Z. Yang, X. Jing, H. Guan, R. Gao and L. Meng, NIR Plasmonic Nanozymes: Synergistic Enhancement Mechanism and Multi-Modal Anti-Infection Applications of MXene/MOFs, *Adv. Mater.*, 2024, **36**, 2307839.

22 N. Solangi, L. Lingamdinne, R. Karri, N. Mubarak, S. Mazari and J. Koduru, Emerging 2D MXene Quantum Dots for Catalytic Conversion of CO_2, *Carbon*, 2025, **232**, 119758.

23 F. Guo, J. Ma, X. Deng and H. Gao, Interface Engineering for Improving Photoelectrocatalytic Performance of 2D/2D MXene@MoS_2 for N_2 Reduction Reaction: A Theoretical Insight, *Fuel*, 2025, **382**, 133704.

24 Z. Zhao, Y. Gao and S. Zhao, Investigation of Electrothermal and Photothermal Actuation Performance in V_2CT_x/PE Composites, *J. Alloys Compd.*, 2025, **1010**, 177333.
25 L. Yu, L. Xu, L. Lu, Z. Alhalili and X. Zhou, Thermal Properties of MXenes and Relevant Applications, *ChemPhysChem*, 2022, **23**, e202200203.
26 Y. Li, M. Lai, M. Hu, S. Zhao, B. Liu and J. Kai, Insights into Electronic and Magnetic Properties of MXenes: From a Fundamental Perspective, *Sustain. Mater. Technol.*, 2022, **34**, e00516.
27 Y. Zhao, J. Wang, D. Yang, Z. Du, X. Zhi, R. Yu, Z. Guo and C. Tang, MXene-CNTs/Co Dielectric-Electromagnetic Synergistic Composites with Multi-Heterogeneous Interfaces for Microwave Absorption, *Carbon*, 2025, **232**, 119825.
28 M. Downes, C. Shuck, B. McBride, J. Busa and Y. Gogotsi, Comprehensive Synthesis of $Ti_3C_2T_x$ from MAX Phase to MXene, *Nat. Protoc.*, 2024, **19**, 1807.
29 Q. Zhang, J. Wang, Q. Yu, Q. Li, R. Fan, C. Li, Y. Fan, C. Zhao, W. Cheng, P. Ji, J. Sheng, C. Zhang, S. Xie, G. Henkelman and H. Li, Metal/MXene Composites via in Situ Reduction, *Sustain. Mater. Technol.*, 2024, **4**, 252.
30 M. Saharudin, A. Ayub, S. Hasbi, F. Muhammad-Sukki, I. Shyha and F. Inam, Recent Advances in MXene Composites Research, Applications and Opportunities, *Mater. Today: Proc.*, 2023, DOI: 10.1016/j.matpr.2023.02.435.
31 P. Li, X. Zhao, Y. Ding, L. Chen, X. Wang and H. Xie, Application Studies on MXene-Based Flexible Composites, *Front. Therm. Eng.*, 2024, **4**, 1440165.
32 Y. Yoon, T. Le, A. Tiwari, I. Kim, M. Barsoum and H. Lee, Low Temperature Solution Synthesis of Reduced Two Dimensional Ti_3C_2 MXenes with Paramagnetic Behaviour, *Nanoscale*, 2018, **10**, 22429.
33 Z. Babar, J. Fatheema, N. Arif, M. Anwar, S. Gul, M. Iqbal and S. Rizwan, Magnetic Phase Transition from Paramagnetic in Nb_2AlC-MAX to Superconductivity-Like Diamagnetic in Nb_2C-MXene: An Experimental and Computational Analysis, *RSC Adv.*, 2020, **10**, 25669.
34 A. Akyildiz, I. Aysan, Y. Abdullahi, B. Hanedar, Z. Vatansever and F. Ersan, Investigation of the Electronic and Magnetic Properties of Bare and Oxygen-Terminated Ordered Double Transition-Metal MXenes for Spintronic Applications, *Phys. Chem. Chem. Phys.*, 2024, **26**, 26566.
35 J. Singh, K. Singh, R. Singh and C. Adetunji, *MXenes: Next-Generation 2D Materials: Fundamentals and Applications*, 2024, pp. 384.
36 X. Jiang, A. Kuklin, A. Baev, Y. Ge, H. Ågren, H. Zhang and P. Prasad, Two-Dimensional MXenes: From Morphological to Optical, Electric, and Magnetic Properties and Applications, *Phys. Rep.*, 2020, **848**, 1.
37 S. Ullah, T. Najam, A. Rehman, S. Alarfaji, M. Ahmad, S. Riaz, B. Akkinepally, S. Shah and M. Nazir, MXene Nanomaterials: Synthesis, Properties and Applications in Energy and Environment Sector, *J. Alloys Compd.*, 2024, **1001**, 175172.
38 Q. Gao and H. Zhang, Magnetic i-MXenes: A New Class of Multifunctional Two-Dimensional Materials, *Nanoscale*, 2020, **12**, 5995.
39 H. Sarmah and S. Ghosh, Surface Passivation and Tunable Magnetic Properties of Cr-Based MXenes, *J. Phys. Chem. C*, 2024, **128**, 16133.
40 S. Ram, N. Koshi, S. Lee and S. Bhattacharjee, Tuning the Electronic and Magnetic Properties of Double Transition Metal ($MCrCT_2$, M = Ti, Mo) Janus MXenes for Enhanced Spintronics and Nanoelectronics, *J. Phys. Chem. C*, 2024, **128**, 7323.
41 M. Khazaei, M. Arai, T. Sasaki, C. Chung, N. Venkataramanan, M. Estili, Y. Sakka and Y. Kawazoe, Novel Electronic and Magnetic Properties of Two-Dimensional Transition Metal Carbides and Nitrides, *Adv. Funct. Mater.*, 2013, **23**, 2185.
42 K. Tan, N. Abdullah, M. Zaed, A. Pandey, A. Zainoodin and R. Saidur, Electrochemical Performance of MXene/Fe_3O_4 Composite Derived from Recycled Carbon for Vanadium Redox Flow Battery, *Fuel*, 2024, **375**, 132574.
43 P. Zhang, N. Sun, R. Soomro, S. Yue, Q. Zhu and B. Xu, Interface-Engineered Fe_3O_4/MXene Heterostructures for Enhanced Lithium-Ion Storage, *ACS Appl. Energy Mater.*, 2021, **4**, 11844.
44 H. Ding, M. Zhang, Y. Liu, Y. Yao, Z. Mai, H. Zheng, B. Song, B. Fan, H. Wang and H. Lu, Synthesis of CS/Fe_3O_4/TiO_2@MXene Nanocomposite Photocatalyst with Excellent Degradation and Bacteriostatic Properties by One-Step Hydrothermal Method, *Ceram. Int.*, 2024, **50**, 46334.
45 A. Alkhudaydi, E. Danish, E. Lima, M. Gabal and M. Salam, Photocatalytic Degradation of Malachite Green Dye Using Ti_3C_2 MXene Nanosheets Decorated with Fe_3O_4 NPs under Visible Light Irradiation, *Res. Chem. Intermed.*, 2024, **50**, 5117.
46 A. Alkhudaydi, B. Samy, E. Danish, E. Lima, M. Gabal and M. Salam, Novel Sensitive Electrochemical Detection of Paracetamol Using Magnetite/MXene Electrode by Differential Pulse Voltammetry, *Int. J. Electrochem. Sci.*, 2024, **19**, 100797.
47 Z. Ma, H. Li, Y. Shen, J. Xu, X. Chen, M. Wu, L. Yang, F. Liu, R. Hao and L. Wang, Highly Selective Capture of Hg(II) Utilizing a MXene-Based Magnetic Cenosphere: Balance on Redox Sites and Magnetism, *Sep. Purif. Technol.*, 2025, **354**, 129073.
48 C. Chen, C. Chang, S. Liaw, C. Lu and J. Chen, Exfoliated MXene Nanosheet by Double Layer Forces for Preparing Magnetic Adsorbents of Toxic Metal Ions and Recycling with Hyperthermic Effect, *Sep. Purif. Technol.*, 2024, **349**, 127855.
49 P. Zhang, H. Li, H. Liang, H. Wang, X. Shan, Y. Wang, X. Fan, K. Xu, Q. Zhang and Y. Chen, Ultra-Lightweight Asymmetric Hierarchical Porous Structure for High-Efficiency Absorption-Dominated Electromagnetic Interference Shielding, *Composites, Part B*, 2025, **290**, 111969.
50 H. Zhang, J. Cheng, K. Liu, S. Jiang, J. Zhang, Q. Wang, C. Lan, H. Jia and Z. Li, Electric-Magnetic Dual-Gradient Structure Design of Thin MXene/Fe_3O_4 Films for Absorption-Dominated Electromagnetic Interference Shielding, *J. Colloid Interface Sci.*, 2025, **678**, 950.

51 W. Lu, Y. Zhou, H. Xu, X. Zhang, Y. Wang and B. Zhao, Dual-Gradient MXene/AgNWs/Hollow-Fe_3O_4/CNF Composite Films for Thermal Management and Electromagnetic Shielding Applications, *Compos. Commun.*, 2024, **51**, 102077.

52 M. Huang, Y. Huang, H. Yang and W. Li, $Ti_3C_2T_x$ MXene/Fe_3O_4/Carbon Fiber Fabric/Water Polyurethane Composite Fabrics for Electromagnetic Interference Shielding and Thermal Management, *ACS Appl. Nano Mater.*, 2024, **7**, 14921.

53 M. Tao, Z. Li and H. Li, Multilayer-Structured MXene/Fe_3O_4 Nanosheets Composites for Electromagnetic Interference Shielding with Low Reflection, *J. Mater. Sci.: Mater. Electron.*, 2024, **35**, 1411.

54 D. Ji, Y. Wang, C. He, K. Cui, P. Han, N. Sun and Y. Li, High-Efficiency Electromagnetic Shielding Based on Multipolar Effect in RGO/MXene Aerogels Decorated with Ordered Fe_3O_4 Cluster, *Carbon*, 2024, **226**, 119189.

55 J. Xu, Z. Wang, C. Ge, X. Qi, Q. Bao and C. Liu, Constructing MXene-Based Mixed-Dimensional Structure with Multiple Interfaces to Optimize Dielectric-Magnetic Synergistic Effect for Effective Electromagnetic Wave Absorption, *J. Colloid Interface Sci.*, 2025, **677**, 529.

56 M. Jia, Q. Chen, K. Chen, X. Zhang, H. Feng, C. Feng, X. Li and D. Zhang, Muscle-Inspired MXene-Based Conductive Hydrogel by Magnetic Induced for Flexible Multifunctional Sensors, *Eur. Polym. J.*, 2024, **214**, 113149.

57 B. Sun, X. Guo, D. Li, J. Zhao, X. Wang, L. Jiang, S. Chen, Y. Zhou, S. Jerrams and F. Zhou, Composites of Non-Woven Poly p-Phenylene Terephthalamide and Fe_3O_4-Decorated $Ti_3C_2T_x$ MXene Nanosheets Coated with Ag Nanoparticles for Electromagnetic Interference Shielding, *ACS Appl. Nano Mater.*, 2024, **7**, 5610.

58 H. Sima, B. Liu, X. Shi, Z. Zhao, C. Liu and C. Zhang, Flexible and Self-Healing Tannic Acid-Fe_3O_4@MXene-Composited Dual Network Hydrogel Multifunctional Strain Sensor, *Colloids Surf., A*, 2024, **702**, 135028.

59 W. Liu, K. Jia, T. Yao, L. Shen and D. Wang, Graphene-Wrapped Magnetic Multichamber $Ti_3C_2T_x$ Spheres for Stable Broadband Microwave Absorption, *ACS Appl. Mater. Interfaces*, 2024, **16**, 51118.

60 J. Huang, H. Sharif, A. Mahmood and C. Li, Unveiling the Heterojunction of Fe_3O_4@MXene Nanocatalyst for Ultrafast Degradation of Antibiotics via Non-Radical Pathway, *Chem. Eng. J.*, 2024, **500**, 156941.

61 J. Shi, J. Chen, X. Wang, Y. Ma, X. Yang, M. Que, H. Yuan, Y. Gao and Y. L, Covalent Assembly of Carboxyl Functionalized $Ti_3C_2T_x$ with Amino-Fe_3O_4 for Excellent Electromagnetic Wave Absorbing Property, *Ceram. Int.*, 2024, **50**, 44793.

62 Z. Hu, W. Zhang, Y. Zhong, Q. Duan, Z. Liu, B. Wang, L. Chen, X. Wang and X. Zhang, MXene-Derived Nano N-TiO_2@MXene Loaded with Fe_3O_4 for Photo-Fenton Synergistic Degradation of Phenol, *ACS Appl. Nano Mater.*, 2024, **7**, 20653.

63 X. Hu, G. Li, Y. Zhang, M. Lu, W. Pu, Y. Dai, M. Yang and H. Wang, A Novel Iron Oxide (Fe_3O_4)-Laden Titanium Carbide (Ti_3C_2) MXene Stacks for the Efficient Removal of Tetracycline from Aqueous Solution, *Chemosphere*, 2024, **364**, 143210.

64 Y. Tang, S. Shao, C. Guo, K. Bi, H. Wang, T. Zhao, J. Liu and F. Wang, Multifunctional Ultralight Magnetic Fe_3O_4@SiO_2/$Ti_3C_2T_x$/rGO Aerogel with Efficient Electromagnetic Wave Absorption and Thermal Management Properties, *Carbon*, 2024, **228**, 119314.

65 S. Yan, S. Shao, Y. Tang, X. Zhang, C. Guo, L. Wang, J. Liu, L. Wu and F. Wang, Ultralight Hierarchical Fe_3O_4/MoS_2/rGO/$Ti_3C_2T_x$ MXene Composite Aerogels for High-Efficiency Electromagnetic Wave Absorption, *ACS Appl. Mater. Interfaces*, 2024, **16**, 36962.

66 J. Jin, S. Wu, X. Fang, H. Li, J. Wang, S. Xuan, W. Kong, D. Wang, X. Chen, K. Leung, Q. Fang and T. Luo, MXene@Fe_3O_4/PDA Nanosheets with Photothermal-Magnetically Coupled Antibacterial Properties, *Mater. Chem. Phys.*, 2024, **322**, 129562.

67 L. Zhuang, Q. You, X. Su, Z. Chang, M. Ge, Q. Mei, L. Yang, W. Dong and L. Li, High-Performance Detection of Exosomes Based on Synergistic Amplification of Amino-Functionalized Fe_3O_4 Nanoparticles and Two-Dimensional MXene Nanosheets, *Sensors*, 2023, **23**, 3508.

68 H. Zeng, X. Du, S. Singh, S. Kulinich, S. Yang, J. He and W. Cai, Nanomaterials via Laser Ablation/Irradiation in Liquid: A Review, *Adv. Funct. Mater.*, 2012, **22**, 1333.

69 W. Qin, X. Hu, J. Fan, Y. Liu, L. Tan, M. Zhou, C. Wu, B. Ge, S. Gao, J. Qian and W. Zhang, One-Step Laser Ablation of Fe Clusters Supported on $Ti_3C_2T_x$ Nanosheets for Enhanced NH_3 Sensing at Room Temperature, *Ceram. Int.*, 2023, **49**, 18353.

70 D. Zhang, B. Gokce and S. Barcikowski, Laser Synthesis and Processing of Colloids: Fundamentals and Applications, *Chem. Rev.*, 2017, **117**, 3990.

71 A. El-Khawaga, A. Zidan, A. Abd El-Mageed, M. Elsayed and M. El-Khawaga, Preparation Methods of Different Nanomaterials for Various Potential Applications: A Review, *J. Mol. Struct.*, 2023, **1281**, 135148.

72 M. Alhabeb, K. Maleski, B. Anasori, P. Lelyukh, L. Clark, S. Sin and Y. Gogotsi, Guidelines for Synthesis and Processing of Two-Dimensional Titanium Carbide ($Ti_3C_2T_x$ MXene), *Chem. Mater.*, 2017, **29**, 7633.

73 P. Rasheed, R. Pandey, T. Gomez, M. Naguib and K. Mahmoud, Large Interlayer Spacing $Nb_4C_3T_x$ (MXene) Promotes the Ultrasensitive Electrochemical Detection of Pb^{2+} on Glassy Carbon Electrodes, *RSC Adv.*, 2020, **10**, 24697.

74 J. Yang, M. Naguib, M. Ghidiu, L. Pan, J. Gu, J. Nanda, J. Halim, Y. Gogotsi and M. Barsoum, Two-Dimensional Nb-Based M_4C_3 Solid Solutions (MXenes), *J. Am. Ceram. Soc.*, 2016, **99**, 660.

75 O. Mashtalir, M. Naguib, V. Mochalin, Y. Dall'Agnese, M. Heon, M. Barsoum and Y. Gogotsi, Intercalation and Delamination of Layered Carbides and Carbonitrides, *Nat. Commun.*, 2013, **4**, 1716.

76 L. Lorencova, T. Bertok, E. Dosekova, A. Holazova, D. Paprckova, A. Vikartovska, V. Sasinkova, J. Filip, P. Kasak, M. Jerigova, D. Velic, K. Mahmoud and J. Tkac, Electrochemical Performance of $Ti_3C_2T_x$ MXene in

Aqueous Media: Towards Ultrasensitive H_2O_2 Sensing, *Electrochim. Acta*, 2017, **235**, 471.

77 P. Michałowski, M. Anayee, T. Mathis, S. Kozdra, A. Wójcik, K. Hantanasirisakul, I. Jóźwik, A. Piątkowska, M. Możdżonek, A. Malinowska, R. Diduszko, E. Wierzbicka and Y. Gogotsi, Oxycarbide MXenes and MAX Phases Identification Using Monoatomic Layer-by-Layer Analysis with Ultralow-Energy Secondary-Ion Mass Spectrometry, *Nat. Nanotechnol.*, 2022, **17**, 1192.

78 C. Patterson, M. Syed and Y. Takemura, Harmonic Decomposition of Magneto-Optical Signal from Suspensions of Superparamagnetic Nanoparticles, *J. Magn. Magn. Mater.*, 2018, **451**, 248.

79 X. Cui, F. Xiang, C. Lu, C. Liu and W. Liu, Magnetic Nanoparticles Detection Based on Nonlinear Faraday Rotation, *Measurement*, 2024, **227**, 114309.

80 M. Becerra and C. Toher, *First-principles Investigation of Surface Functionalization and CO_2 Adsorption in MXenes, NM01.07.16*, MRS Spring Meeting & Exhibit, 2024.

81 J. Björk and J. Rosen, Functionalizing MXenes by Tailoring Surface Terminations in Different Chemical Environments, *Chem. Mater.*, 2021, **33**, 9108.

82 C. Gu, W. Weng, C. Lu, P. Tan, Y. Jiang, Q. Zhang, X. Liu and L. Sun, Decorating MXene with tiny ZIF-8 nanoparticles: An effective approach to construct composites for water pollutant removal, *Chin. J. Chem. Eng.*, 2022, **42**, 42.

83 T. Yamashita and P. Hayes, Analysis of XPS Spectra of Fe^{2+} and Fe^{3+} Ions in Oxide Materials, *Appl. Surf. Sci.*, 2008, **254**, 2441.

84 V. Svetlichnyi, A. Shabalina, I. Lapin, D. Goncharova, D. Velikanov and A. Sokolov, Characterization and Magnetic Properties Study for Magnetite Nanoparticles Obtained by Pulsed Laser Ablation in Water, *Appl. Phys. A*, 2017, **123**, 763.

85 A. De Bonis, T. Lovaglio, A. Galasso, A. Santagata and R. Teghil, Iron and Iron Oxide Nanoparticles Obtained by Ultra-Short Laser Ablation in Liquid, *Appl. Surf. Sci.*, 2015, **353**, 433.

86 H. Aye, S. Choopun and T. Chairuangsri, Influence of Solvents on Characteristics of Nanoparticles Prepared by Pulsed Laser Ablation on Iron Target, *Chiang Mai Univ. J. Nat. Sci.*, 2014, **13**, 37.

87 V. Amendola, D. Amans, Y. Ishikawa, N. Koshizaki, S. Scirè, G. Compagnini, S. Reichenberger and S. Barcikowski, Room-Temperature Laser Synthesis in Liquid of Oxide, Metal-Oxide Core-Shells, and Doped Oxide Nanoparticles, *Chem.–Eur. J.*, 2020, **26**, 9206.

88 P. Rasheed, R. Pandey, T. Gomez, K. Jabbar, K. Prenger, M. Naguib, B. Aïssa and K. Mahmoud, Nb-Based MXenes for Efficient Electrochemical Sensing of Small Biomolecules in the Anodic Potential, *Electrochem. Commun.*, 2020, **119**, 106811.

89 S. Zhao, X. Wang, N. Kurra, Y. Gogotsi and Y. Gao, Effect of Pinholes in Nb_4C_3 MXene Sheets on its Electrochemical Behavior in Aqueous Electrolytes, *Electrochem. Commun.*, 2022, **142**, 107380.

90 V. Gajdosova, L. Lorencova, M. Prochazka, M. Omastova, M. Micusik, S. Prochazkova, F. Kveton, M. Jerigova, D. Velic, P. Kasak and J. Tkac, Remarkable Differences in the Voltammetric Response Towards Hydrogen Peroxide, Oxygen and $Ru(NH_3)_6^{3+}$ of Electrode Interfaces Modified with HF or LiF-HCl Etched $Ti_3C_2T_x$ MXene, *Microchim. Acta*, 2019, **187**, 52.

91 A. Bard, L. Faulkner and H. White, *Electrochemical methods: fundamentals and applications*, John Wiley & Sons, 2022, pp. 1104.

92 L. Lorencova, V. Gajdosova, S. Hroncekova, T. Bertok, M. Jerigova, D. Velic, P. Sobolciak, I. Krupa, P. Kasak and J. Tkac, Electrochemical Investigation of Interfacial Properties of $Ti_3C_2T_x$ MXene Modified by Aryldiazonium Betaine Derivatives, *Front. Chem.*, 2020, **8**, 553.

93 J. Aguedo, Z. Pakanova, L. Lorencova, M. Nemcovic, P. Kasak, M. Barath, P. Farkas and J. Tkac, MXene as a Novel Cartridge for N-Glycan Enrichment, *Anal. Chim. Acta*, 2022, **1234**, 340512.